J. Fluid Mech. (2006), *vol.* 560, *pp.* 123–147.
doi:10.1017/S0022112006000656 Printed in the United Kingdom

The wake of a cylinder performing rotary oscillations

By B. THIRIA[1], S. GOUJON-DURAND[1,2] AND J. E. WESFREID[1]

[1]Physique et Mécanique des Milieux Hétérogènes, Ecole Supérieure de Physique et Chimie Industrielles de Paris (PMMH UMR 7636 CNRS-ESPCI-P6-P7), 10 rue Vauquelin, 75231 Paris, Cedex 5, France

[2]Université Paris XII, Créteil, France

(Received 22 February 2005 and in revised form 20 December 2005)

We study the wake of a cylinder performing rotary oscillations around its axis at moderate Reynolds number. We observe that the structure of the vortex shedding is strongly affected by the forcing parameters. The forced wake is characterized by a 'lock-in' region where the vortices are shed at the forcing frequency and a region where the vortices can be reorganized to give a second frequency close to those observed for the unforced wake. We show that these modifications of the wake structure change the dynamic of the fluctuations downstream from the cylinder. We vary the amplitude and the frequency of the oscillations and study the consequences of these modifications on the mean flow and the global drag applied on the cylinder. We then discuss the mechanism responsible for the modification of the fluctuations and the modification of the drag coefficient.

1. Introduction

Control of vortex shedding has been of great interest in the last decade. From the practical point of view, controlling shedding in the wake addresses two fundamental industrial preoccupations. First, for synchronized open flow such as the Bénard–von Kármán instability, vortex shedding induces vibrations on the structure owing to the fluctuations of lift and secondly, it is known that the drag depends strongly on the fluctuations of the perturbed flow. Reducing the strength of vortices shed is thus a way of reducing vibrations and drag. Among the various ways to reduce vortex shedding, one consists of applying appropriate oscillatory temporal forcing to the wake. Some properties of oscillatory flows are reported in reviews by Berger & Willie (1972) and Bearman (1984). In the particular case of a cross-flow past a circular cylinder, the effect of 'in-line' oscillations on wake structure and hydrodynamic forces have been the subject of many numerical works such as Blackburn & Henderson (1999) and Guilmineau & Queutey (2002) and experimental works by Sarpkaya & Isaacson (1981), Carberry, Sheridan & Rockwell (2001) and Williamson & Roshko (1988).

In the present work, the periodic forcing studied is an oscillating rotating motion around the cylinder axis specified by its azimuthal velocity and its forcing frequency as was first visualized by Taneda (1978). In their experimental study, Tokumaru & Dimotakis (1991) proposed that the rotary oscillation of the cylinder could, for optimal parameters, achieve a significant drag reduction (80 %) at a Reynolds number of 15 000. The drag coefficient as a function of the forcing parameters was deduced from the variations of the wake displacement thickness calculated from streamwise mean velocity profiles. Several numerical calculations described this dependence of drag on the forcing parameters such as those conducted by Shiels & Leonard (2001), who

explored the effects of rotary oscillations for a range of Reynolds number from 150 to 15 000 and confirmed the strong decrease in drag for the same Reynolds number as Tokumaru & Dimotakis (1991), but observed that the forcing was less effective at lower Reynolds-numbers. The Reynold-number dependence of the efficiency of the control was also observed by Choi, Choi & Kang (2002) who studied numerically the effect of the oscillating motion of the circular cylinder on the mean drag reduction for Reynolds numbers 100 and 1000 which, respectively, passed from 12 % to 60 %. Concerning the behaviour of the wake characteristics under forcing conditions, several numerical studies were conducted such as those by Baek, Lee & Sung (2001), and Baek & Sung (2000), who studied the secondary and tertiary lock-on of the lift coefficient for small values of forcing amplitude. Cheng, Chew & Luo (2001*a*) gave in their paper a detailed study of the flow pattern modifications occurring at and close to lock-on. In addition, the flow behind an oscillatory cylinder has been a model for flow control and optimization (see He *et al.* 2000; Protas & Styczek 2002; Smith, Siegel & McLaughlin 2002).

Several explanations of the physical mechanisms responsible for drag reduction have been proposed: from Shiels & Leonard (2001), it seems that the decrease in drag comes from a time-averaged separation delay initiated by an appropriate rotational oscillation. Protas & Wesfreid (2002, 2003) proposed in a numerical investigation at $Re = 150$ that the modification of the drag was directly correlated to the mean flow correction (zeroth mode, see Zielinska *et al.* 1997) caused by the forcing through the action of the divergence of the Reynolds stress tensor of the fluctuating forced flow.

The first challenge of this present study was to perform experimentally direct drag measurements, which is delicate for a body in motion and for efforts of this order of magnitude at our Reynolds number. Direct experimental measurements of the global drag have not yet been performed except by Fujisawa, Ikemoto & Nagaya (1998) in the same configuration, but for higher Reynolds number ($Re = 20\,000$) and by integrating the pressure distribution over the cylinder surface for small amplitude of the oscillation. In the present study, the Reynolds number is $Re = 150$, the same as that studied by Protas & Wesfreid (2002, 2003) in their numerical simulation, but it is assumed that the physical mechanisms remain the same for a larger range. The goal of this paper is to determine, from the direct drag measurements, a link between the modification of the dynamics of the forced wake for a large range of amplitudes and frequencies of the rotary oscillating motion, and the modification of the mean drag coefficient.

The present paper is structured as follows. In the first section we present the evolution of the global wake patterns as a function of the forcing parameters from flow visualizations. Then we present the drag measurements performed in our hydrodynamic tunnel as well as the spatial distributions of the fluctuations in the forced wakes. We discuss the relation between these experimental results as an explanation for the dependence of the drag regarding the wake patterns. In the last section, we give the physical mechanism which is responsible for the wake characteristics modifications and which is known as *vorticity control.*

2. Experimental set-up

2.1. *Control parameters*

We study the flow behind an oscillatory cylinder which rotates around its axis according to

$$\theta(t) = \theta_0 \cos(\omega_f t),$$

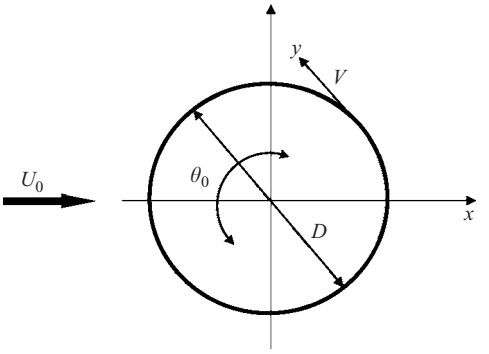

FIGURE 1. Control parameters of the oscillating motion.

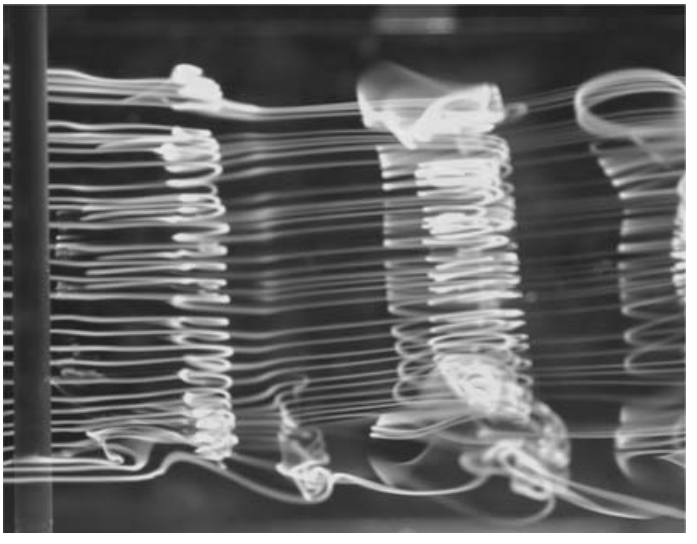

FIGURE 2. Typical streakline visualization in the (x, z)-plane of the wake under forcing conditions. No characteristic spanwise variation can be observed for a large part of the hydrodynamic tunnel cross-section when the cylinder oscillates.

where ω_f is the angular forcing frequency,

$$\omega_f = 2\pi f_f.$$

We define the forcing amplitude as

$$A = V_{max}/U_0,$$

where $V_{max} = (D/2)\theta_0\omega_f$ is the maximal azimuthal velocity of the forced oscillation (where D is the diameter of the cylinder), and the upstream velocity is U_0 (figure 1). Finally, we define f_0 as the vortex-shedding frequency of the unforced wake at the same Reynolds number. We only have two non-dimensional forcing parameters which are defined by A and the ratio f_f/f_0. The natural frequency of vortex shedding is about 0.98 Hz for $Re = 150$.

From Poncet (2002, 2004), and as observed in our hydrodynamic tunnel, the cylinder oscillation produces a strong coherent forcing along the cylinder span which diminishes the possible spanwise variations due to three-dimensional instabilities or end effects. The visualization in the plane of the cylinder under forcing conditions (figure 2)

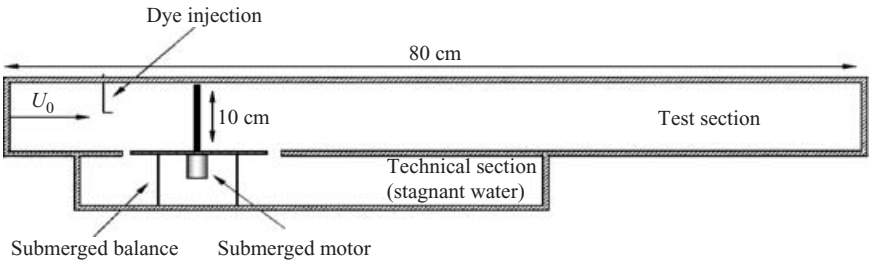

FIGURE 3. Test section of the hydrodynamic tunnel.

has been taken in our tunnel and shows that the wake structure does not present spanwise variations for a large part of the test cross-section. It appears that the hypothesis of a two-dimensional flow is then a reasonable approximation.

2.2. *Description of the hydrodynamic tunnel*

Our experiments were performed in a low-velocity water tunnel, built with transparent Plexiglas walls, with a 10 cm × 10 cm cross-section and a typical velocity $U_0 = 3\,\mathrm{cm\,s^{-1}}$. The circular cylinder has a diameter of $D = 0.5$ cm which corresponds, for our typical velocity, to a Reynolds number $Re = U_0 D/\nu = 150$, where ν is the kinematic viscosity. The tunnel is equipped with a technical section placed just under the test section. This section is entirely filled with water and interconnected with the test section as shown in figure 3 and allows us to instrument the cylinder directly without passing through the Plexiglas walls and to put measuring instruments such as a balance in it, which is normally impossible in classical hydrodynamic tunnels.

Rotation was produced by a computer-controlled brushless d.c. submerged motor and was transferred to the obstacle through a transmission mechanism. The wake visualizations were performed in the (x, y)-plane using laser induced fluorescence (LIF) technic. The laser sheet is realized by putting a cylindrical lens in front of the laser beam from an argon ion laser. The dye (fluorescein dye in solution) was injected on both sides of the centreline in the middle of the tunnel at $y = \pm D/2$, upstream from the cylinder. The dye was delivered using two small capillary tubes which are sufficiently far from the cylinder and sufficiently thin (0.07 cm) to prevent their own wakes from affecting the mean flow for our typical velocity. We have measured the velocity fields in the same (x, y)-plane as the wake visualizations. We used a standard particle image velocimetry set-up (PIV) from *LaVision*®. The flow was seeded with spherical particles of a typical diameter of 11 µm. The typical extension of the PIV images were about $30D$ going from $x = -5D$ to $x = 25D$ if we take the origin at the centre of the cylinder cross-section. For all the PIV measurements, we used a 16×16 interrogation window with an overlap of 50 % which gives a spatial resolution of 22 360 velocity vectors for each field obtained.

2.3. *Hydrodynamic balance*

One particularity of our hydrodynamic tunnel is that we can directly measure the drag F_x on the rotating cylinder. As shown in figure 4, the bluff body is placed on a plate supported by two thin brass blades of 0.02 cm thick which is free to move in the streamwise direction. The space around the plate which allows it to move is sufficiently thin (less than 0.03 cm) not to affect the principal flow. Four floats filled with air are placed under the plate in order to offset the weight of the plate, the motor and the cylinder. Gauge sensors of extensiometry from *Vishay*® were glued on one of the

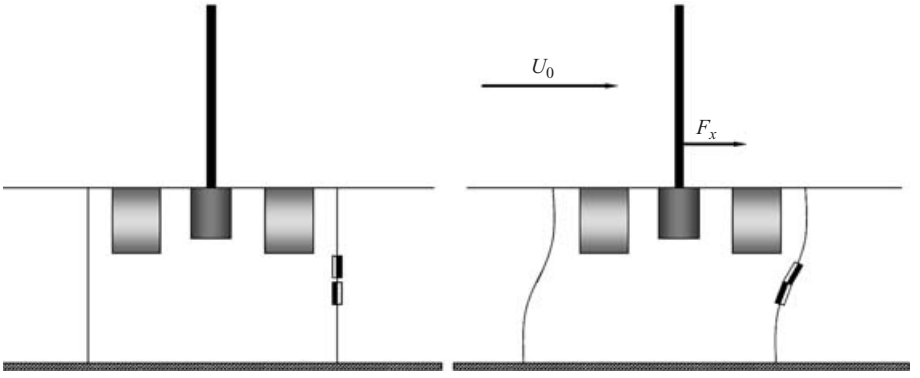

FIGURE 4. Schematic view of the submerged balance with the floats and the gauges sensors.

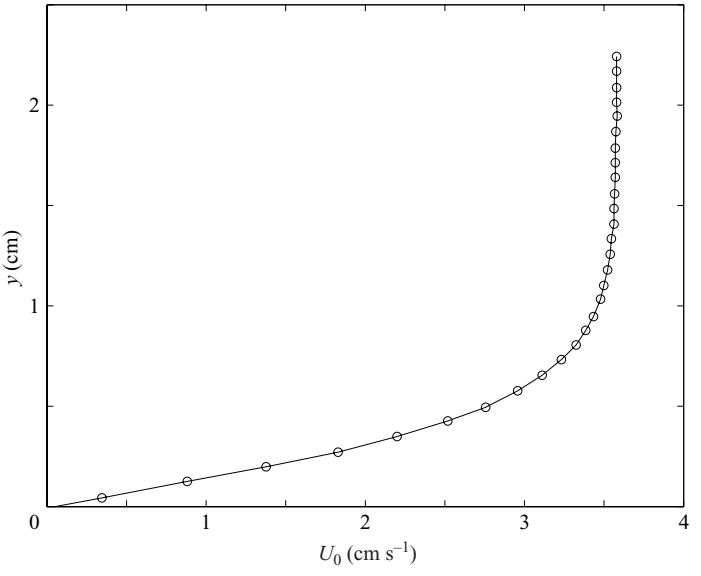

FIGURE 5. Velocity profile measured by PIV one diameter upstream from the cylinder at $z = D/2$. The boundary-layer thickness is estimated at 1 cm.

two blades. When a flow is applied to the bluff body, the two blades become warped and there is an electric signal due to the deformation of the gauge sensors plugged with a Wheatstone bridge from *Vishay*® and proportional to the force suffered by the cylinder. Typical forces on the cylinder are of the order of 0.20 mN. However, the cutoff frequency of this system which is less than 1 Hz, allows us to measure only mean drag. Nevertheless, the advantage of this prototype of a submerged balance is that it allows us to measure values of mean forces with a precision of 0.01 mN.

Finally, the boundary-layer thickness was estimated by measuring a velocity profile one diameter upstream of the cylinder (figure 5). The tunnel has a square cross-section, and the profile can be measured in the y or z direction. From figure 5, the boundary-layer thickness was found to be near 1 cm. Thus, it appears that a non-negligible part of the cylinder span ($\sim$10 % of each side) is located in the tunnel boundary layers. This implies that the drag measurement, which corresponds to the global force integrated along the whole cylinder span, takes into account the boundary-layer

effects. However, the goal of this paper is to study experimentally the effect of the cylinder oscillation on the global drag for a given Reynolds number, so with constant boundary layers. Thus, for a study of the relative drag as a function of the forcing parameters, it appears that these measurements are sufficient to describe precisely the influence of the forcing on drag.

3. Wake visualizations

3.1. *Effect of the forcing frequency on wake pattern*

We performed a series of wake visualizations using LIF as a function of the forcing parameters. Figure 6 shows, for a fixed forcing amplitude ($A = 2$), the evolution of the shedding pattern as a function of the forcing frequency. We chose this typical value of A which allows the exploration of a wide range of physical behaviours (high and low drag) as a function of the forced frequency.†

For the different forcing frequencies, the forced wake presents the same characteristics: the vortices are shed at the forcing frequency in the near wake (as flapping vortices). For $f_f/f_0 > 1$ (figure 6*c*–*f*), we can see that these vortices merge in the far wake from both rows to give a new pattern similar to that observed for the unforced case. This behaviour has been observed numerically in different numerical simulations such as Lu & Sato (1996), Chou (2001) and Choi, Choi & Kang (2002). This composite pattern has been also observed by Nishihara, Kanedo & Watanabe (2005) in the case of a circular cylinder oscillating longitudinally in the streamwise direction, which shows that this behaviour can be reproduced in forced wakes in general. The extension at which the vortices present a quasi-stable pattern corresponding to the forcing frequency is strongly dependent on the value of this frequency. This spatial lock-in length decreases as the forcing frequency increases. (In this paper, the term 'lock-in', which is generally used to distinguish the particular case of forcing $f_f/f_0 = 1$ in the literature, is employed to characterize the zone containing shedding structures at the forcing frequency.) However, in cases where $f_f/f_0 \leqslant 1$ (figure 6*a*, *b*), the forced pattern persists along the tunnel length, the shed vortices do not interact and no pattern similar to the unforced case is recovered. Far away, the streaklines do not show a coherent structure.

3.2. *Effect of the forcing amplitude on wake pattern*

As we did to study the effect of the forcing frequency on the vortex shedding, we fixed f_f/f_0 and varied the forcing amplitude A; the flow visualizations of the wake patterns are shown in figure 7. The value of the forcing frequency was fixed at $f_f/f_0 = 5$ in order to have a short lock-in length at low amplitude and not to be limited by the length of the channel. We studied the full evolution of the flow patterns in the range of forcing amplitude $0 < A < 10$. As we will see in § 4, these forcing conditions correspond to a low drag situation.

The lock-in length is also strongly influenced by the amplitude of the cylinder motion. For a first range of forcing amplitude, the lock-in region grows with the amplitude A reaching a maximum. Above this value, which for the forcing frequency $f_f/f_0 = 5$ and this Reynolds number is near $A = 5$, it starts to decrease as we continue to increase the forcing amplitude. For a sufficiently strong amplitude, the forced wake has almost recovered the shedding pattern of the unforced case. This dependence on the forcing amplitude is observed for all the forcing frequencies studied, but, as was

† Movies of streaklines visualizations for each pair of forcing parameters used in this work $0.5 < f_f/f_0 < 6$ and $1 < A < 10$ can be found at http://ftp.espci.fr/shadow/thiriaJFM05.

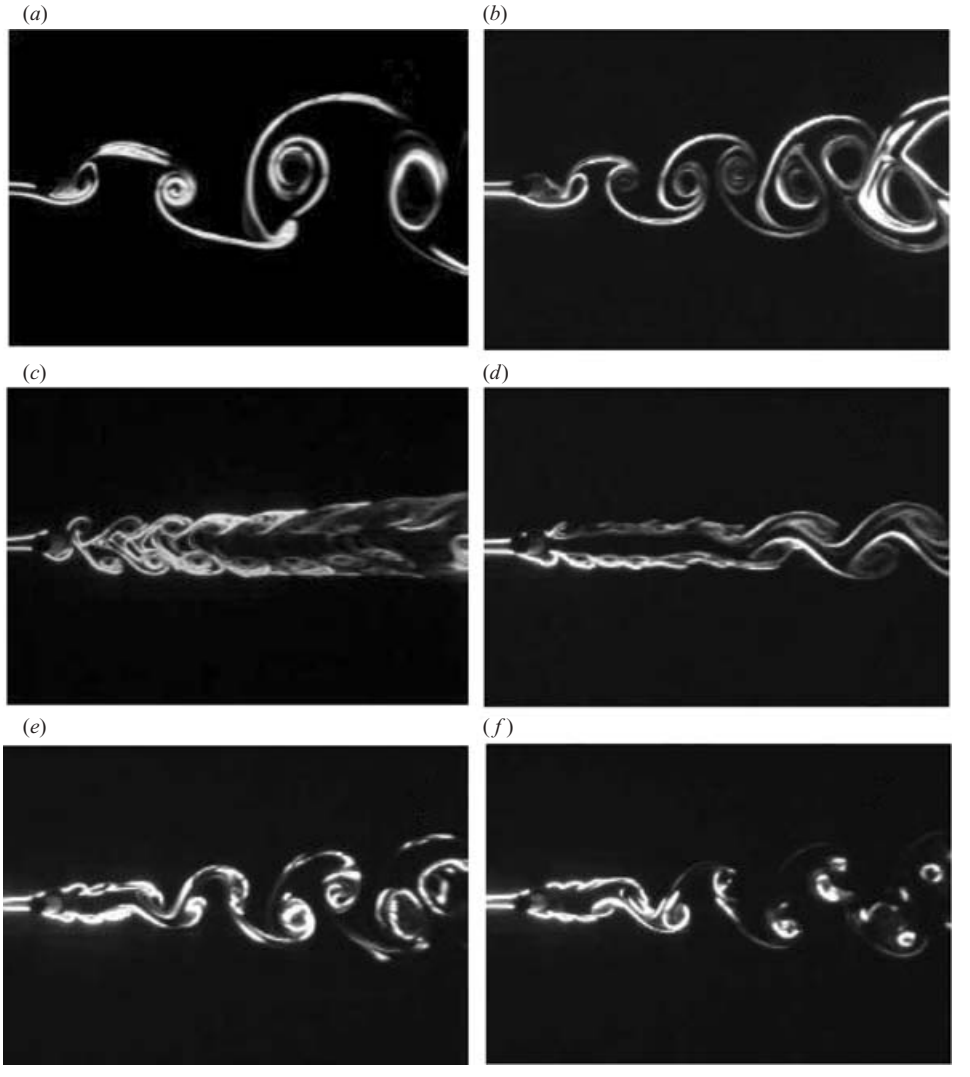

FIGURE 6. Effect of the forcing frequency on the wake at constant forcing amplitude $A = 2$. The forcing frequency is (*a*) $f_f/f_0 = 0.5$, (*b*) $f_f/f_0 = 1$, (*c*) $f_f/f_0 = 2$, (*d*) $f_f/f_0 = 3$, (*e*) $f_f/f_0 = 4$ and (*f*) $f_f/f_0 = 5$. The vortices are shed at the forcing frequency in the near wake and for $f_f/f_0 > 1$ merge from each row to give a new pattern in the far wake similar to that observed for the unforced case with a frequency slightly lower than the unforced one. This typical lock-in length decreases as f_f/f_0 increases.

shown in figure 6, the effective length for a fixed forcing amplitude changes with the forcing frequency.

The physical mechanisms responsible for the transition between the first near-wake shedding pattern which comes from the forcing and the second far-wake shedding pattern have been studied by Thiria & Wesfreid (2006) in the framework of global linear stability analysis under forcing conditions. In this study, they show that the dynamics of the re-emergent pattern (and so the near-wake pattern) are intrinsically related to a change in the spatio-temporal characteristics of the global instability of the flow owing to the strong mean flow correction induced by the forcing and which can lead, for strong forcing, to a globally stable flow (i.e. the only characteristic

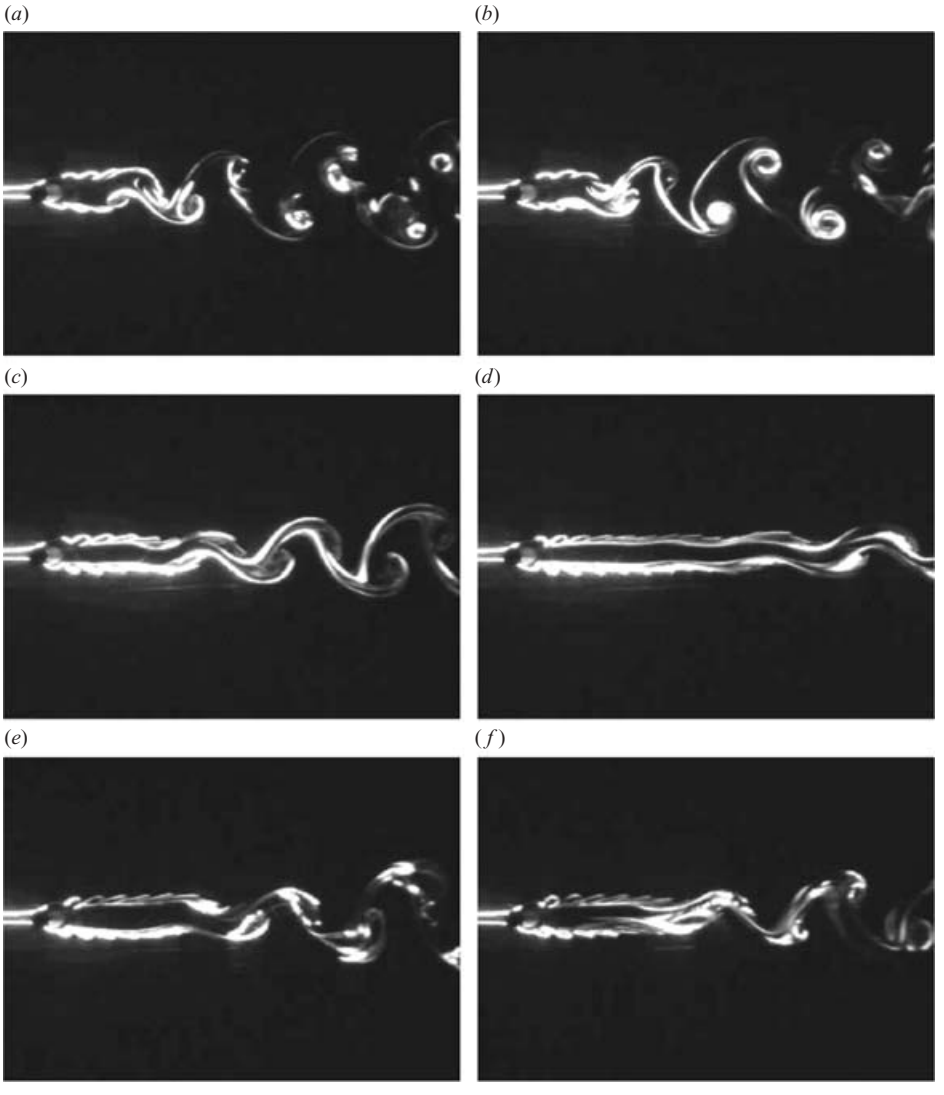

FIGURE 7. Effect of the forcing amplitude on the wake. The forcing frequency is $f_f/f_0 = 5$ (low-drag situation), the forcing amplitude is (*a*) $A = 1$, (*b*) $A = 2$, (*c*) $A = 4$, (*d*) $A = 5$, (*e*) $A = 7$ and (*f*) $A = 9$. In the near wake, the vortex shedding is excited at the forcing frequency and the far wake shows a re-emergent pattern similar to the natural one.

pattern of the wake is the forced near-wake pattern, see figure 7*c*). In the following study, the evolution of the lock-in region as a function of the forcing parameters will be discussed only in relation to drag measurements.

4. Drag measurements

We performed drag measurements with our hydrodynamic balance as a function of the forcing parameters at $Re = 150$. Figure 8 shows the evolution of the ratio between the mean drag measured under forcing and the drag measured with no control (cylinder at rest). For each forcing frequency, this value was determined as the ratio of the signal obtained when the cylinder oscillates, and when the rotation is switched

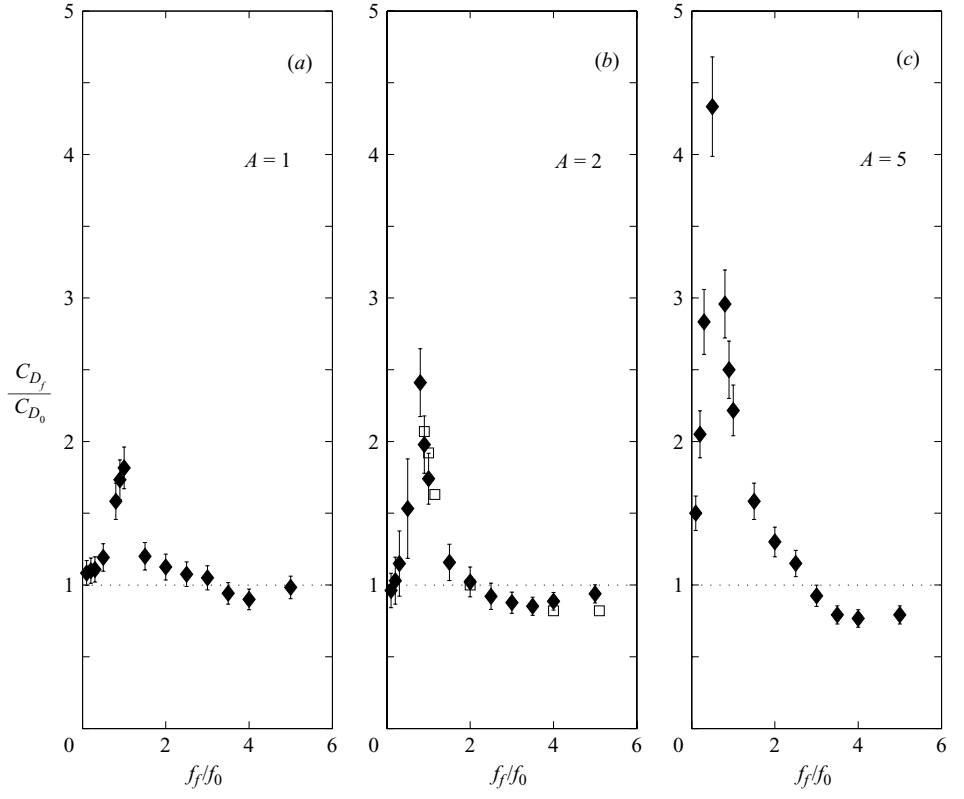

FIGURE 8. Variation of the mean drag coefficient C_{Df}/C_{D_0} as a function of the non-dimensional forcing frequency for (*a*) $A=1$, (*b*) $A=2$ and (*c*) $A=5$. For high amplitude A, the drag reduction can reach 25 % and drag amplification near 400 %. The location of the most substantial drag amplification shifts to smaller frequencies as forcing amplitude grows. The dashed line corresponds to the drag with no forcing. The numerical results for $A=2$ from Protas & Wesfreid (2002) (□) have been added for comparison.

off. The results are plotted as a function of the forcing frequency and for different forcing amplitudes: $A=1$, $A=2$ and $A=5$. The first observation to be made is that the global drag is affected by the forcing conditions and that the measurements with our submerged balance are precise enough to detect small changes in these modifications. While looking at a single curve, we can see that the drag coefficient has a sharp maximum and a wide minimum. This coefficient is defined as $C_D = F_x/\frac{1}{2}\rho U_0^2 S$, where ρ is the fluid density and S the surface defined by $S=Dl$ where l is the cylinder length. C_{D_f} and C_{D_0} are, respectively, the drag coefficient obtained under forcing and no forcing conditions. The value of the drag starts to increase with forcing frequency until its maximum value which corresponds to a forcing frequency close to the resonant case ($f_f/f_0 \lesssim 1$). From this value, the drag coefficient decreases with f_f/f_0 and for a sufficiently large frequency, we can see drag reduction. Once the minimum value of drag is reached, C_{D_f} starts to increase again with the forcing frequency and tends to C_{D_0}.

These results are in qualitative agreement with those found by He *et al.* (2000) and Cheng, Liu & Lam (2001*b*) for $Re=200$, and experimentally by Tokumaru & Dimotakis (1991) for a higher Reynolds number (15 000) and quantitative agreement with those obtained numerically by Protas & Wesfreid (2002) for forcing amplitude $A=2$ (figure 8*b*).

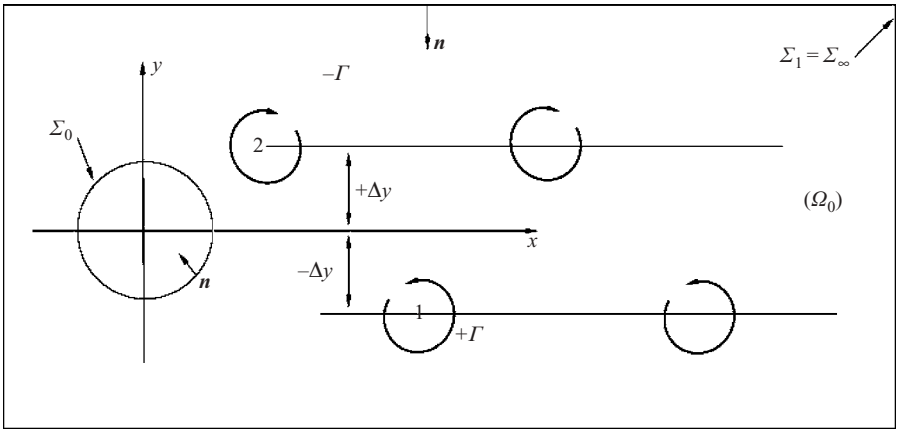

FIGURE 9. Definition of the control volume enclosing the body and extended to Σ_1 and 'Point vortex' schematization of the Bénard–von Kármán vortex street.

If we increase the forcing amplitude A, the variations in the measured drag become more pronounced. The maximum value of drag is over four times the value of the unforced case for the forcing amplitude $A = 5$ (figure 8*c*). On the other hand, the drag is reduced as we increase f_f/f_0. For this forcing amplitude, the drag reduction observed is about 25 % for an optimal forcing frequency near $f_f/f_0 = 4$–5. These parameters are in good agreement with those reported by He *et al.* (2000) and Bergmann (2004) for a slightly higher Reynolds number ($Re = 200$): $f_f/f_0 \simeq 4$ and $A \simeq 4$. The maximum drag reduction is much less than those observed by Tokumaru & Dimotakis (1991), who obtained a drag reduction of near 80 % at $Re = 15\,000$ estimated in term of the streamwise momentum flux for a given control volume, or from Lu & Sato (1996) who observed numerically a drag reduction of more than 50 % at $Re = 1000$. According to Choi *et al.* (2002), who studied numerically the effect of rotary oscillation on drag for two different Reynolds number (100 and 1000), it appeared that the effect of the forcing on the drag coefficient was strongly Reynolds-number dependent even if the physical mechanisms are the same.

The location of the maximum and minimum value of drag depends on the forcing amplitude. From figure 8(*a*) to 8(*c*), we can see that the location of the most substantial drag amplification shifts to smaller frequencies as forcing amplitude grows. This means that for higher forcing amplitudes, the high-drag situation does not correspond to resonant forcing ($f_f/f_0 = 1$).

4.1. *Hydrodynamic forces*

As was observed in the previous section, the forcing conditions strongly affect the drag coefficient and each modification of the drag corresponds to a radical change in the spatial characteristic of the wake pattern. Therefore, in order to understand the effects of the rotary oscillation on the force acting on the body (i.e. the contribution of the shed pattern to global drag), we chose to adopt an approach for the drag which takes into account the unsteady and spatial characteristics of the wake.

One way to express the hydrodynamic forces acting on a body is to consider the impulse relation as was done by Saffman (1992) and recently revisited by Noca, Shiels & Jeon (1999) or Rockwell (2000) for a finite control volume (i.e. in order to estimate directly the hydrodynamic forces from PIV velocity fields) (figure 9). If we write the momentum balance for a geometric control volume Ω_0 including the

body and extended to infinity and if the fluid density is set to one ($\rho = 1$), that the hydrodynamic force for a two-dimensional flow can be expressed as follows:

$$\boldsymbol{F} = -\frac{\mathrm{d}}{\mathrm{d}t}\int_{\Omega_0} \boldsymbol{r} \times \boldsymbol{\omega}\,\mathrm{d}\Omega + \frac{\mathrm{d}}{\mathrm{d}t}\oint_{\Sigma_0} \boldsymbol{r} \times (\boldsymbol{n} \times \boldsymbol{V})\,\mathrm{d}\sigma. \tag{4.1}$$

It can easily be shown that the second term on the right-hand side taken over the contour Σ_0 of (4.1) is equal to 0 in the case of a rotating cylinder. We finally obtain for the expression of the hydrodynamic forces:

$$\boldsymbol{F} = -\frac{\mathrm{d}}{\mathrm{d}t}\int_{\Omega_0} (\boldsymbol{r} \times \boldsymbol{\omega})\,\mathrm{d}\Omega. \tag{4.2}$$

This formula associates the force with the time derivative of the vorticity impulse. As can be seen, the hydrodynamic forces are intrinsically dependent on the spatial distribution of the vorticity in the entire control volume Ω_0. If we consider the special case of a staggered array of counter-rotating point vortices as used to model the Bénard–von Kármán vortex street (figure 9), equation (4.2) can be approximated for the drag component by (Protas & Wesfreid 2003):

$$F_x \cong -\frac{\mathrm{d}}{\mathrm{d}t}\sum_i \Gamma_i \Delta y_i = -\frac{\mathrm{d}}{\mathrm{d}t}[(+\Gamma_1)(-\Delta y_1) + (-\Gamma_2)(+\Delta y_2) + \cdots], \tag{4.3}$$

where Γ_i and Δy_i are now the circulation and the location, respectively, of the vortex above (or below) the centreline. In our case, the vortices above the centreline ($+\Delta y_i$) correspond to negative values of Γ_i and conversely the vortices below the centreline ($-\Delta y_i$) have positive circulation Γ_i.

Considering expression (4.3), each vortex contributes in the same way (depending on its circulation and its position from the centreline) to the global drag force. With this model in mind, we analyse in the next section the vorticity distribution of the forced wakes.

5. Particle image velocimetry measurements

5.1. *Near wake instantaneous vorticity field*

We performed PIV measurements of the near wake of the cylinder using a measurement window between $x = 0$ and $x = 5D$ for different forcing conditions. The forcing amplitude has been fixed to $A = 5$ corresponding to the most significant changes in the drag coefficient (figure 8*c*). The vorticity fields are displayed in figure 10 as a function of the forcing frequency from $f_f/f_0 = 0.5$ to $f_f/f_0 = 5$. The flow fields shown in figure 10 have been obtained by phase averaging 200 snapshots of the flow field obtained by periodic sampling. This phase averaging was obtained by synchronization between the angular position of the cylinder controlled by computer and the laser pulses.

As we could expect, the first observation of these vorticity fields show clearly that the distribution of vorticity in the near wake is strongly affected by the forcing frequency, as has been observed in the streakline evolution displayed in figure 6 for $A = 2$. Except for the first case corresponding to higher drag ($f_f/f_0 = 0.5$) which is particular and will be discussed later, we see that the evolution of the near wake as a function of the forcing frequency (from $f_f/f_0 = 1$ to $f_f/f_0 = 5$) is characterized by two distinct effects due to the rotary oscillation. On the one hand, and as the

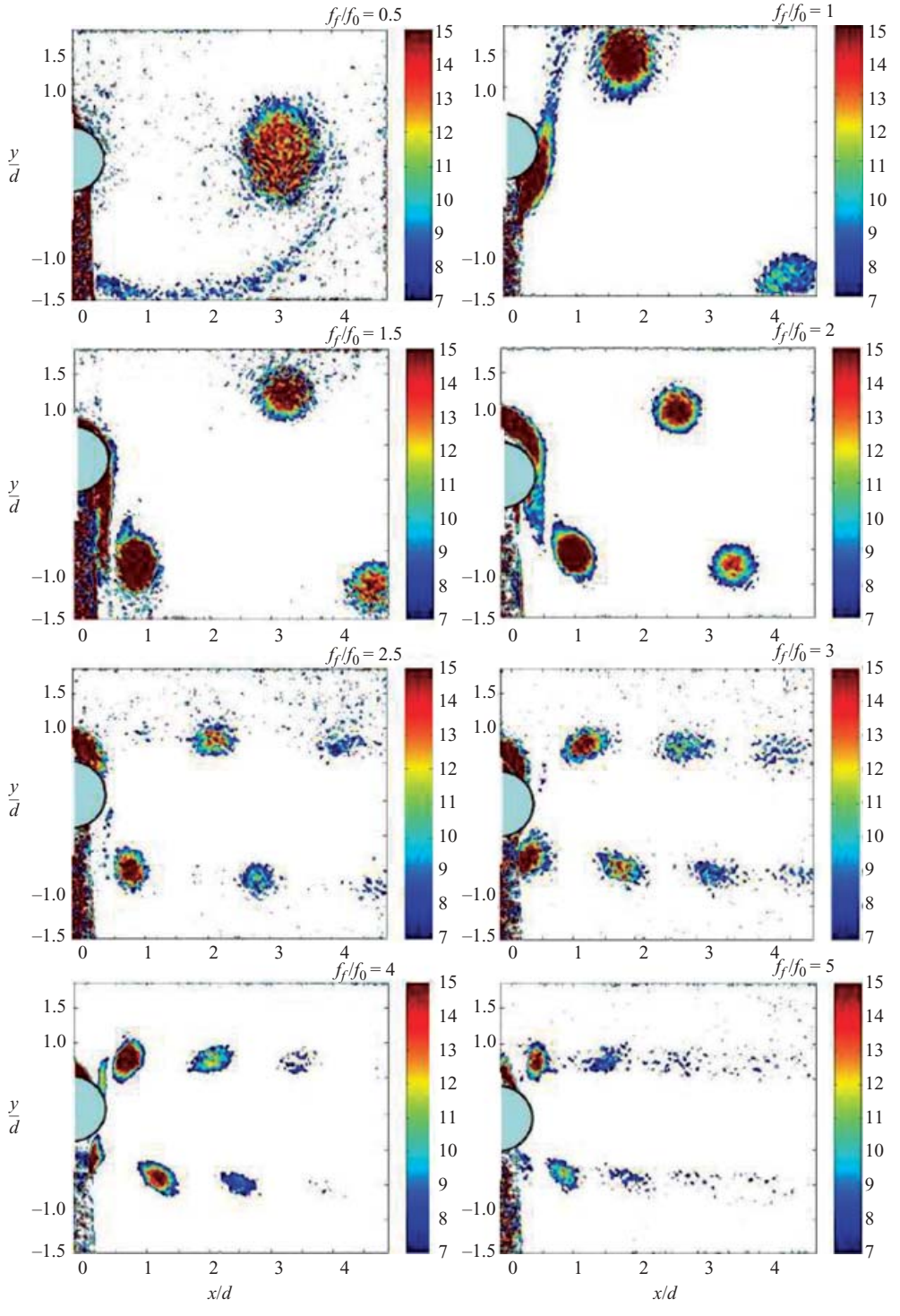

FIGURE 10. Evolution of the instantaneous vorticity fields in the near wake as a function of the forcing frequency. The forcing amplitude is $A = 5$. As f_f/f_0 increases, the vortices shed in the near-wake become weaker and come close to the centreline. These figures should be compared with the streaklines displayed in figure 6 (for $A = 2$) and the drag curve displayed in figure 8*c*).

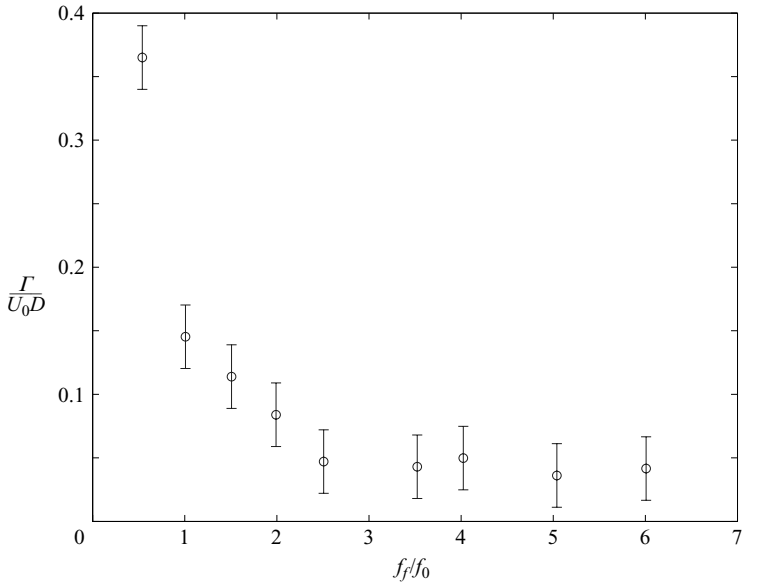

FIGURE 11. Evolution of the circulation Γ calculated on the closest shed vortex as a function of the forcing frequency. The forcing amplitude is $A = 5$.

forcing frequency increases, the vortices shed by the cylinder lose intensity, passing from strong structures to very weak structures, thus decreasing the circulation Γ of each vortex. On the other hand, during this evolution, the eddies shed approach the centreline $y = 0$, thus decreasing the distance $\Delta(y)$ of each vortex from the centreline. The modification of these two properties of the wake are displayed in figure 11, where the circulation is obtained by integrating the vorticity flux on the closest shed vortex and figure 12 as a function of the forcing frequency. This situation corresponds to the transition from high drag to low drag. Thus, the action of the control on the wake structure and then the drag becomes more clear: according to relations (4.2) and (4.3), the rotating oscillation, by recasting the vorticity in the near wake, combines two complementary effects playing a fundamental role in the drag expression. In most patterns displayed in figure 10, it is observed that increasing the forcing frequency (i.e. going from drag amplification to drag reduction situations) diminishes the distance between the vortex rows and circulation of each eddy shed, so the drag. However, the case corresponding to the higher drag (as observed in figure 8*c* for $f_f/f_0 = 0.5$ and $A = 5$), is a characteristic example where the link between the shedding pattern and the drag becomes more complicated. The centres of the vortices are very close to the centreline, which contradicts what has been previously written for the other cases. The difficulty lies in the fact that the drag expression (4.2) involves a time derivative and requires knowledge of the vortex formation process, as was discussed by Jeon & Gharib (2004). A simple snapshot of the vorticity field cannot *a priori* account for the instantaneous value of the drag which is, in fact, dictated by its dynamic in time. However, for most of the observed patterns in figure 10, the shed vortices quickly take their positions above (or below) the centreline and keep their distance from the centreline as a function of space. In those cases, (4.3) can be very useful as a guide to the physical understanding of the effect of the control and the contribution of the near wake to drag, but is not complete since the case $f_f/f_0 = 0.5$, $A = 5$ presents a

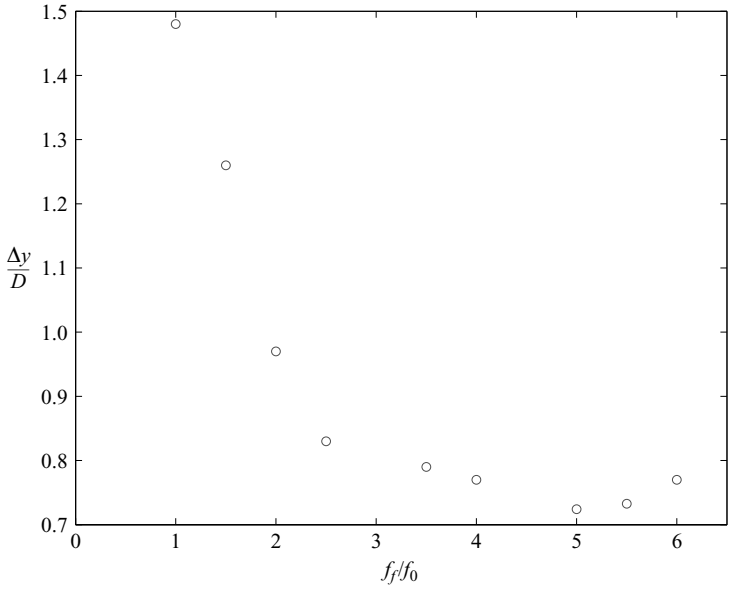

FIGURE 12. Evolution of the vortex position from the centreline ($y = 0$) as a function of the forcing frequency. The forcing amplitude is $A = 5$.

different dynamic. For this case, the evaluation of the contribution of the near wake to global drag would require knowledge of its complete evolution in time (which is more complicated with our experimental set-up). However, from the drag measurements shown in figure 8, we can expect that the considerable amplification of the circulation of these structures is responsible for the strong increase in drag.

5.2. *Distribution of fluctuations in the entire wake*

The previous results concerned the near wake. We investigated the spatial distribution of fluctuation velocity by studying the r.m.s. fields (field of the fluctuating component of the velocity $u' = \sqrt{u_x'^2 + u_y'^2}$) obtained by PIV at the centreline ($y = 0$) with a measurement window covering more than 25 cylinder diameters using 250 instantaneous velocity fields sampled at 2 Hz for each pair of forcing parameters. This number of fields was found to be sufficient to obtain a well-converged mean flow. The evolution of the spatial envelope of these fluctuations (where the envelope describes the amplitude of $u'(x, y, t)$ as a function of x) from the free case to the drag reduction situation (i.e. for forcing frequency $f_f/f_0 = 5$ as a function of the forcing amplitude) is shown in figure 13.

The envelope observed for the unforced case is representative of the global mode amplitude which has been the subject of many studies over the past ten years. (Indeed, the global mode envelope is obtained in the unforced case only with the transversal component of velocity u_y at $y = 0$ or the longitudinal component u_x at $y = y_{max}$ where this latter is maximal (see Wesfreid, Goujon-Durand & Zielinska 1996). Here, the full r.m.s. field is very near to the representation of the envelope obtained with u_y.) A review of the principal studies on the subject has been presented by Chomaz (2005). Zielinska & Wesfreid (1995), Goujon-Durand, Jenffer & Wesfreid (1994) and Wesfreid, Goujon-Durand & Zielinska (1996) investigated numerically and experimentally this global mode in the case of Bénard–von Kármán instability and found scaling laws for the x and y components of the fluctuating part of the velocity u'. Thiria & Wesfreid

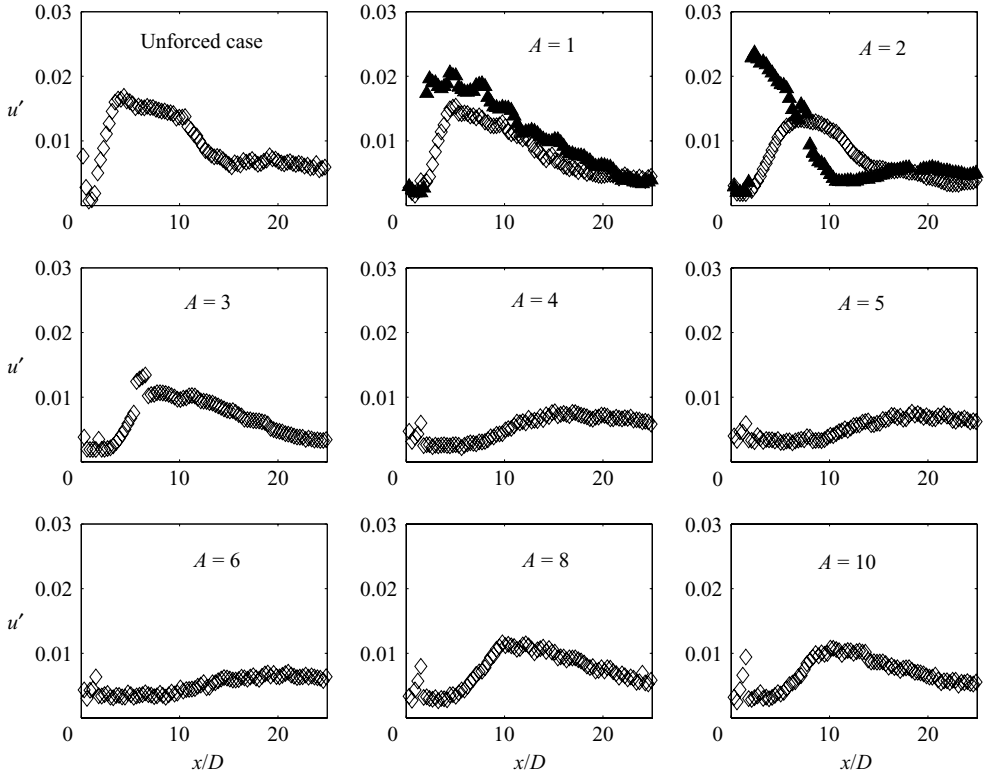

FIGURE 13. ◇, Shapes of the spatial envelope (r.m.s value of the velocity in the wake as a function of space) as a function of the forcing amplitude for the low-drag situation ($f_f/f_0 = 5$). The distribution of the fluctuations globally decreases and the front between the near-wake lock-in wave and the far-wake wave is spatially pushed back as the forcing amplitude increases. Two shapes corresponding to high drag are also plotted ($f_f/f_0 = 1$ for $A = 1$ and $A = 2$ and are indicated by ▲).

(2006) study the stability and the scaling laws of these modified global modes under forcing. For the following, we will consider these shapes only as a footprint of the velocity fluctuation field as a function of space.

The envelope of this mixed mode (with forced frequency near the body in the lock-in region and frequency near to those observed for the unforced case in the far wake) changes its form as a function of the forcing amplitude. The front between the near-wake lock-in wave and the far-wake wave which is, at low forcing, sharp and relatively close to the body, is then spatially pushed back as we increase the forcing amplitude, and the global spatial distribution of the velocity fluctuations becomes weaker. The distance from the body to the front corresponds to the lock-in length examined in the previous section. Beyond this point, the recovered shape of velocity fluctuations, which presents qualitatively the same characteristics as the unforced case, is related to the far-wake pattern of vortices.

According to the flow visualizations, and applying the conclusions of formula (4.3), the drag depends on the contributions of the two observed wake patterns: the near-wake forced shed pattern and the re-emerging one in the far-wake. In term of drag reduction, it becomes evident that the extent of the lock-in region is of great importance. For frequencies close to $f_f/f_0 = 5$, where one can observe the strongest drag reductions, the lock-in region is that with the weakest intensity.

For our Reynolds number, it seems that it is impossible to obtain a semi-infinite vortex street shed at the forcing frequency promoting the best drag reduction. The two shear layers present behind the cylinder owing to the presence of the body must be destabilized to give the re-emerging pattern. The existence of this pattern explains why it is less efficient to reduce drag than to amplify it, since the control parameters in this case only push back (without suppressing) the position of the global shedding front by modification of the mean flow.

For further comparison, we plotted two of the r.m.s. distributions corresponding to the high-drag situation in figure 13 ($f_f/f_0 = 1$ for $A = 1$ and $A = 2$) which are indicated by filled triangles. These distributions exhibit a behaviour opposite to that of the low-drag frequency. The front is closer to the body and indicates a more violent dynamic of fluctuations, and the global fluctuations in the wake increase. Furthermore, and because we are in a lock-in regime, all the modification of the fluctuations due to the motion of the body is employed to increase the drag. Comparison can be done between the case $f_f/f_0 = 1$ and $f_f/f_0 = 5$ for $A = 2$ in figure 13. For forcing frequency $f_f/f_0 = 5$, the re-emergent pattern exists while it is not present for $f_f/f_0 = 1$ and the only important velocity perturbations are given by the forcing in the near wake where strong lock-in exists.

If the physical mechanism for control of fluctuations in wake by rotary oscillations is the same over a large range of Reynolds number, we can suggest that the high performance obtained for higher Reynolds number (Tokumaru & Dimotakis 1991; Shiels & Leonard 2001) are probably due to an effective lock-in length much greater than we can reach for $Re = 150$. More precisely, it seems that the so-called lock-on regime studied by Baek & Sung (2000), Baek *et al.* (2001) and Cheng *et al.* (2001*a*) (i.e. the regime where the whole wake oscillates at the only forcing frequency, corresponding in our work to a semi-infinite lock-in length) is particularly easily reached when the Reynolds number is large. Nevertheless, the dependence of the lock-in boundary as a function of the Reynolds number is still an open question.

6. High-speed camera visualizations

We have seen in the last section that rotary oscillations had a large influence on the global fluctuations in the wake. In order to understand the mechanism underlying this situation, we measured the phase lag between the forcing and the shedding vortices. Wake visualizations were performed in the near wake of the cylinder with a high-speed digital camera (KODAK®). The angular position of the cylinder can be followed in time by painting a mark on the top of the cylinder. We fixed the forcing amplitude to $A = 2$, performing the experiment only as a function of the forcing frequency. The camera frequency acquisition was set for 250 pictures per second in order to obtain a good decomposition of the motion of the wake. The main features of the experiments have shown clearly that the phase lag varied with forcing frequency.

Figure 14 shows the evolution of the wake during the formation of one vortex in the lower row for $f_f/f_0 = 1$. During a half period, the position and the rotating direction of the cylinder is marked by a paint mark and an arrow, respectively, on each picture composing the evolution of the wake. The pictures show that the motion of the first vortex (corresponding to positive circulation Γ) is counter-rotative with the rotating motion of the cylinder during the entire half-period. By increasing the forcing frequency, the dynamic of the forced wake changes. The forcing frequency in the experiment observed in figure 15 is $f_f/f_0 = 1.5$. As in the preceding case, we follow the evolution of the wake from a vortex formation in the lower row. During the first

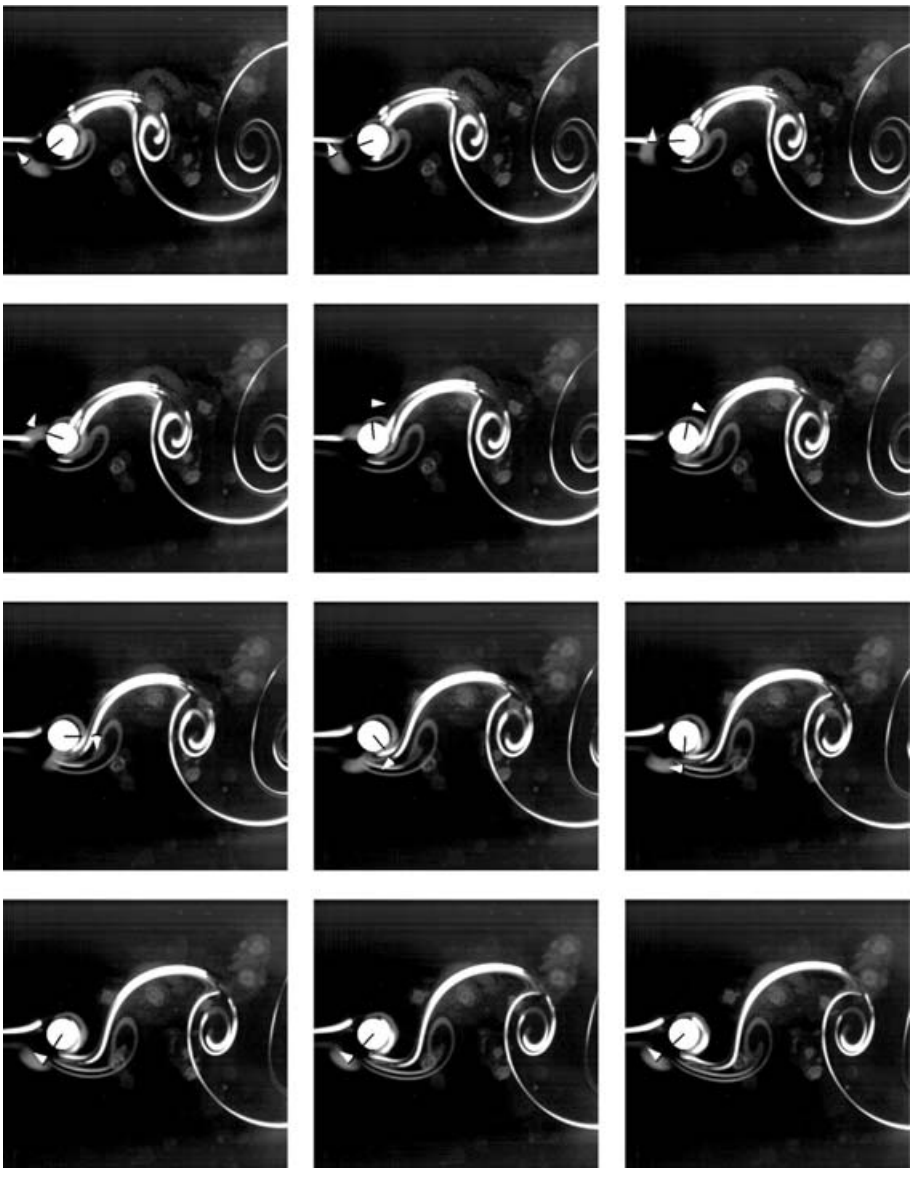

FIGURE 14. Evolution of the wake during a half-period of vortex shedding (i.e the time from the birth of a vortex in the lower row to the birth of the next one in the upper row). The forcing frequency is $f_f/f_0 = 1$, and the corresponding forcing amplitude is $A = 2$. The black line indicates the position of the paint mark on the cylinder and the white arrow indicates its direction. During the whole half-period, the motion of the cylinder is counter-rotative with the nearest vortex (constructive case). The time interval between each pair of pictures is $t = 0.08$ s.

moments of the formation of this vortex, the cylinder rotates in the direction opposite to that of the nearest ejected vortex as we observed for the resonant case, shown in figure 14. When the cylinder changes direction, for the rest of the half-period, the motion of the cylinder is co-rotative with that of the first vortex in the lower row. Figure 16 displays the same visualizations for a higher frequency of the oscillation, where one can observe drag reduction ($f_f/f_0 = 3$). In this case, for the whole

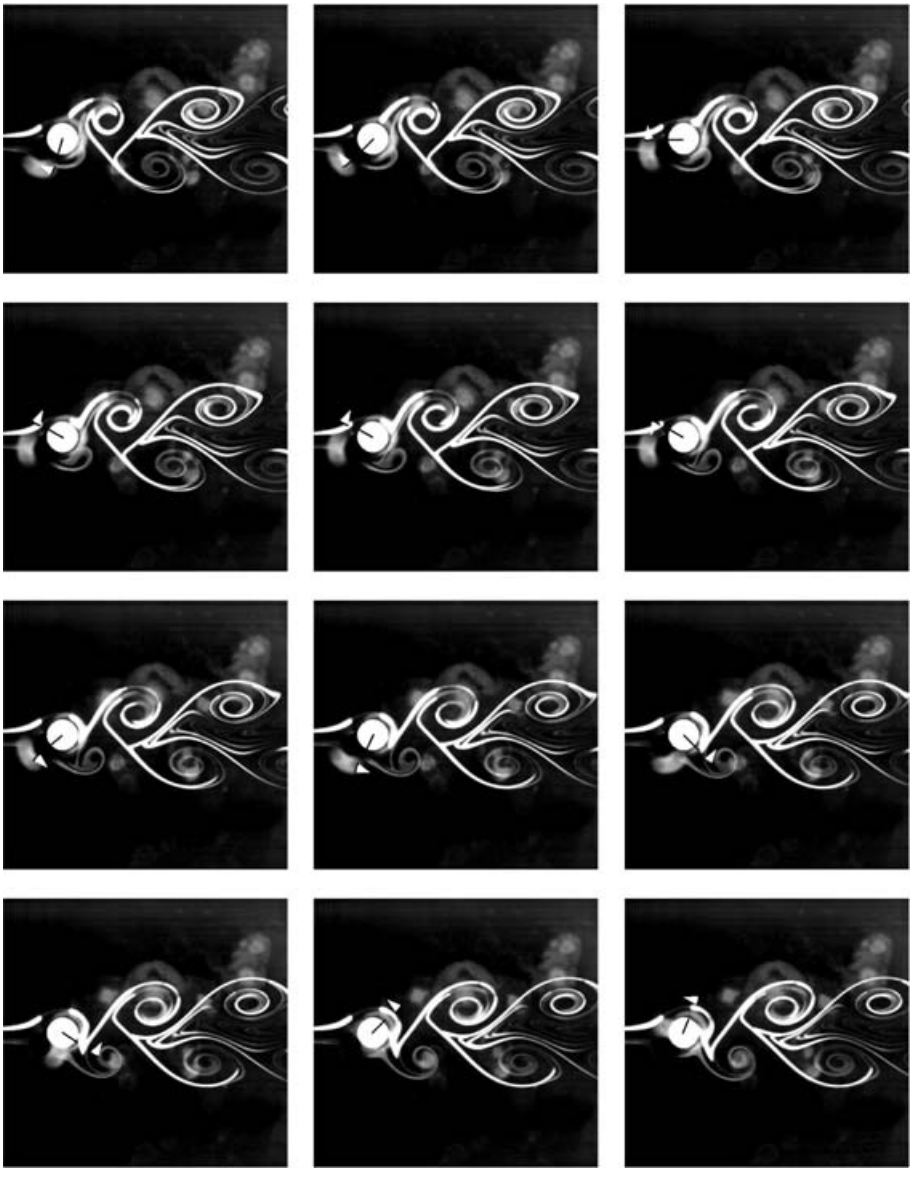

FIGURE 15. Evolution of the wake during a half-period of vortex shedding (i.e the time from the birth of a vortex in the lower row to the birth of the next one in the upper row). The forcing frequency is $f_f/f_0 = 1.5$, and the corresponding forcing amplitude is $A = 2$. The black line indicates the position of the paint mark on the cylinder and the white arrow indicates its direction. From pictures one to five (from left to right and top to bottom), the motion of the cylinder is counter-rotative with the nearest vortex (constructive case as observed in the resonant case). From picture six, the cylinder changes its direction until the end of the half-period, the motion of the cylinder and the nearest vortex are co-rotative (destructive case). The time interval between each pair of pictures is $t = 0.054$ s.

half-period of vortex shedding, the motion of the cylinder and those of the closest vortex become co-rotating. These simple observations may explain how the rotating motion of the cylinder can affect the vorticity distribution in the near-wake. From the two typical cases displayed in figures 14 and 16 (i.e. the completely counter-rotating

FIGURE 16. Evolution of the wake during a half-period of vortex shedding (i.e the time from the birth of a vortex in the lower row to the birth of the next one in the upper row). The forcing frequency is $f_f/f_0 = 3$ (corresponding to drag reduction situation), and the corresponding forcing amplitude is $A = 2$. The black line indicates the position of the paint mark on the cylinder and the white arrow indicates its direction. During the whole half-period, the motion of the cylinder is co-rotative with the nearest vortex (destructive case). The time interval between each pair of pictures is $t = 0.027$ s.

and co-rotating cases), we can distinguish two types of interaction. The first case, relating to the complete counter-rotating motion between the cylinder and the closest vortex, can be seen as a constructive interaction. In this case, the cylinder moves in the opposite direction to the vortex in the boundary layer. The circulation induced by the cylinder motion is of the same sign as the circulation of this vortex and then interacts constructively. Thus, the circulation of each vortex shed every half-period is

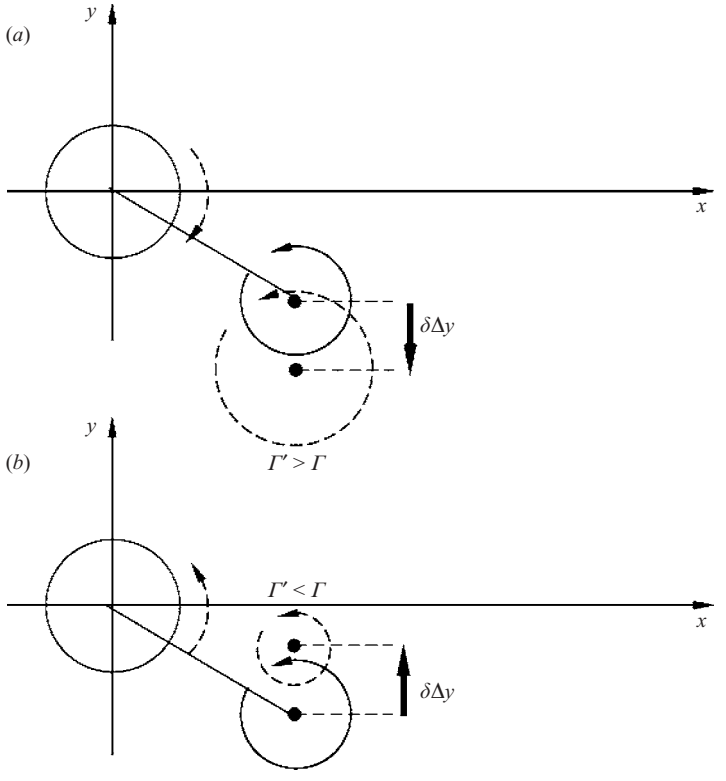

FIGURE 17. Representation of (*a*) the constructive case, when the rotating motions of the cylinder and the nearest vortex are counter-rotating (*b*) and the destructive case, when the rotating motions of the cylinder and the nearest vortex are co-rotating.

amplified. In contrast, if these two motions are co-rotating (figure 16), the circulation created by the cylinder motion is of opposite sign to that of the forming vortex and leads this time to a destructive interaction. In addition, while moving, the cylinder plays the role of an angular velocity distribution in the flow field and we can again distinguish two cases of interaction. In one case, a complete counter-rotating motion of the cylinder induces in the closest vortex, a velocity tending to displace it from the centreline. Conversely, a complete co-rotating motion tends to make it approach the centreline in the case of a co-rotating motion.

This principle, illustrated in figure 17, recalls the basis of the mechanism known as vorticity control, which consists of injecting unsteady vortices interacting with those existing in the wake and which has been discussed by Barrett *et al.* (1999) and Zhu *et al.* (2002) in the case of fish-like locomotion studies. They observed that the drag coefficient of their fish-like body was strongly dependent on the interaction between the vortices shed from the separation lines and the oscillation of the articulated caudal fin. They distinguished, as we do in the present paper, a destructive interference case where drag is reduced and a constructive interference case where the drag increases.

We have generalized this study of the behaviour observed in figures 14, 15 and 16 to the range of forcing frequency from 1 to 5 times the natural shedding frequency (from the high-drag situation to the low-drag situation). The phases of the motions of the cylinder and the closest vortex were determined by reconstituting the two sinusoidal motions as a function of time using several spatio-temporal diagrams at

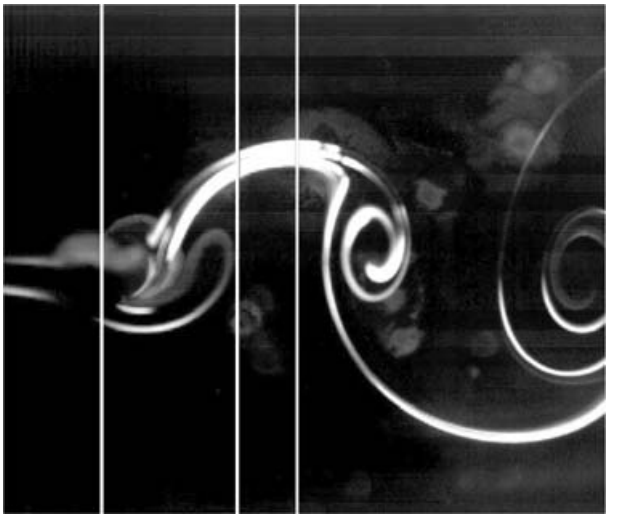

FIGURE 18. Locations of the different 'probes' used for spatio-temporal diagrams.

different locations in the near-wake for each series of fast camera visualizations. The first spatio-temporal diagram was taken at the location of the paint mark on the cylinder as shown in figure 18. The result allowed us to determine directly the position of the cylinder as a function of time, but we were unable to detect the exact time at which the vortex was shed near the cylinder. However, to determine the phase of the vortex shedding, we studied two spatio-temporal diagrams in two different locations downstream from the cylinder. Between these two locations, we deduced the advection velocity of the vortex V_{adv}. From V_{adv}, we deduced the time spent by the vortex in travelling from the cylinder to the first location and then the phase lag due to advection ϕ_{adv}, with

$$\phi_{adv} = \frac{2\pi}{T}\left(\frac{x_{first\ location} - x_{origin}}{V_{adv}}\right).$$

The evolution of the phase lag ϕ between the rotating motion of the cylinder and the vortex shedding plotted in figure 19 is obtained from the phase

$$\phi_c = \omega_f t$$

of the sinusoidally rotating cylinder and the phase

$$\phi_v = (\omega_f t - \phi_{adv})$$

of the nearest vortex shed.

As can be observed in figure 14, when the phase lag ϕ for the resonant case is close to π, the velocity induced by the motion of the cylinder gives a constructive contribution to that induced by the closest vortex. This constructive contribution involves a global increase to the fluctuation part of the velocity field, which increases the circulation and in consequence, the drag. As we increase the forcing frequency, the phase lag ϕ starts to decrease. In this case, the contribution of the cylinder during a half-period of vortex shedding is alternatively constructive and destructive. When the forcing becomes sufficiently important, the phase lag ϕ tends to 0; the contribution of the rotating motion of the cylinder becomes completely destructive to the closest vortex. Contrary to what we observe for the resonant case, the consequences are that

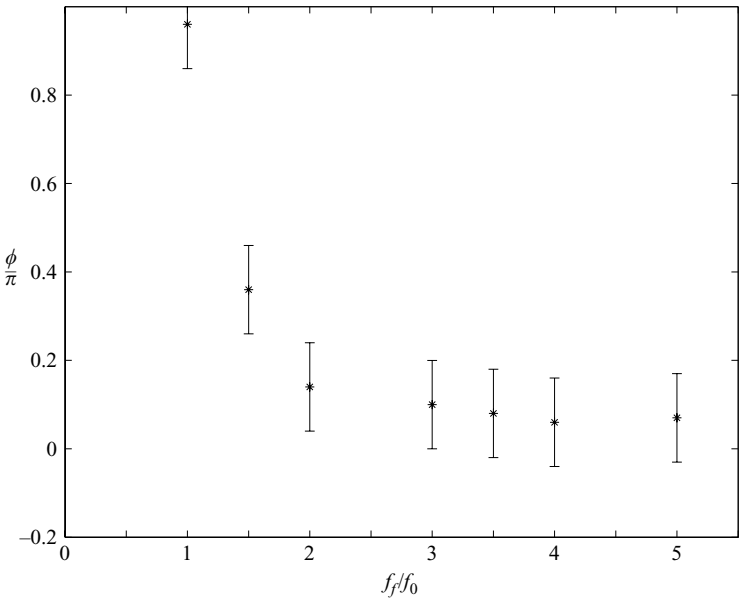

FIGURE 19. Phase lag between the rotating motion of the cylinder and the vortex shedding as a function of the forcing frequency. For the resonant case, the motion of the cylinder is counter-rotating with the closest vortex $\phi/\pi \simeq 1$. As we increase the forcing frequency, the phase lag tends to 0, the motion of the cylinder becomes co-rotating with the closest vortex. The forcing amplitude is $A = 2$.

the fluctuations in the flow field are globally weaker than in the natural case. It is important to note that the constructive (or destructive) contribution of the rotating motion of the cylinder is, of course, dependent on its amplitude. For this experiment, the forcing amplitude was fixed at $A = 2$; if we increase the amplitude, the global fluctuations in the wake (and thus the drag) can be greater (or weaker), as we saw from the drag and PIV measurements.

6.1. *Discussion*

It appears that the mechanism responsible for reduction or amplification of the fluctuations in the wake is that known as vorticity control. The oscillating cylinder plays the role of an additional vortex which interacts with those in the vortex street. The phase lag between the vortex shedding and the sinusoidal motion of the cylinder which depends on the forcing parameters can give either a global constructive or destructive contribution to the wake vortices which explains why the fluctuations in the wake can be amplified or reduced. As shown in figure 8, the forcing frequency corresponding to the maximum (and minimum) drag is a function of the forcing amplitude. According to our reasoning, the optimum phase lags for the two extreme cases (the high-drag situation which corresponds to a fully counter-rotating motion between the cylinder and the closest vortex and the low-drag situation which corresponds to a fully co-rotative motion) should naturally follow the forcing frequency of these two optima in drag. For a forcing amplitude $A = 5$, the phase lag corresponding to the fully constructive case ($\phi \backsimeq \pi$) was found for a forcing frequency near $f_f/f_0 = 0.5$ which corresponds indeed to the maximum value of drag found in figure 8(*c*), while the value of $\phi \backsimeq 0$ was found for a forcing frequency where one observes the best drag reduction ($f_f/f_0 \backsimeq 4$–5). Table 1 shows the optimal values (higher drag amplification

A	$(C_{Df}/C_{D0\,extremum})$	$(f_f/f_{0\,extremum})$	ϕ
2	1.8	1	π
2	0.9	3–5	0
5	4.3	0.5	π
5	0.75	4–5	0

TABLE 1. Optimal drag coefficients (in the sense of maximal or minimal drag coefficient) and their corresponding forcing frequency as a function of forcing amplitude ($A = 2$ and $A = 5$). The last column shows the phase lag measured for these optimal frequencies.

and better drag reduction) of the drag coefficient and the phase ϕ corresponding to these cases.

We conclude that vorticity control appears to be one of the mechanisms which is responsible for the drag modification. However, the fact that the phase lag between the vortex shedding and the cylinder motion changes with the forcing is still an open problem. As the phase lag is also strongly dependent on the forcing amplitude, we presume that it is also Reynolds-number dependent which could explain why the optimal parameters for drag reduction (or amplification) vary with the upstream velocity (cf. Tokumaru & Dimotakis 1991; Choi *et al.* 2002).

7. Conclusion

In this paper, we present the first direct drag measurements for a rotating oscillating cylinder at $Re = 150$. We confirm the strong dependence of this coefficient as a function of the forcing parameters: the ratio A of the azimuthal velocity of the cylinder surface with the upstream velocity and the ratio between the forced and natural frequencies of the vortex shedding. We have performed direct visualizations of the vortex shedding and we have observed the space distribution of velocity fluctuations and vorticity. We correlated the drag modification of a cylinder performing rotary oscillations with the vorticity control and we have shown that the injection of external vorticity of adequate sign modifies the near-wake field. The phase lag between the vortex shedding and the rotary motion of the cylinder gives either a constructive contribution to the wake which is responsible for a global decrease in the fluctuations in the wake, or a destructive contribution which gives the opposite behaviour. According to the impulse formula (cf. Saffman 1992), the drag coefficient is directly correlated to the wake pattern which is consistent with our results on global modes and drag. The aim of this paper was to focus on the unsteady characteristics of the wake, but it was observed that the modification of the fluctuations affects the mean flow as was discussed by Protas & Wesfreid (2002). The fact that the drag reduction seems to come from time-averaged separation delay (Shiels & Leonard 2001) or from a modification of the Reynolds stress can be interpreted as a consequence of the mechanism described in this paper.

We would like to acknowledge D. Pradal, D. Vallet, J. C. Guibert, P. Jenffer and M. de Saint Aubert for their invaluable assistance concerning the experimental set-up and O. Cadot, B. Protas, C. Mitescu and J. F. Beaudoin for fruitful discussions.

This work was supported by Schlumberger in Clamart, France.

REFERENCES

Baek, S.-J., Lee, S. B. & Sung, H. J. 2001 Response of a circular cylinder wake to superharmonic excitation. *J. Fluid Mech.* **442**, 67–88.

Baek, S.-J. & Sung, H. J. 2000 Quasi-periodicity in the wake of a rotationally oscillating cylinder. *J. Fluid Mech.* **408**, 275–300.

Barrett, D. S., Triantafyllou, M. S, Yue, D. K. P., Grosenbauch, M. A. & Wolfgang, M. J. 1999 Drag reduction in fish-like locomotion. *J. Fluid Mech.* **392**, 183–212.

Bearman, P. W. 1984 Vortex shedding from oscillating bluff bodies. *Annu. Rev. Fluid Mech.* **16**, 195–222.

Berger, E. & Willie, R. 1972 Periodic flow phenomena. *Annu. Rev. Fluid Mech.* **4**, 313–340.

Bergmann, M. 2004 Optimistation aérodynamique par réduction de modeles POD et contrôle optimal. Application au sillage laminaire d'un cylindre circulaire. PhD thesis, Inst. Natl Polytech. Lorraine, Nancy-France.

Blackburn, H. M. & Henderson, R. D. 1999 A study of two-dimensional flow past an oscillating cylinder. *J. Fluid Mech.* **385**, 255–286.

Carberry, J., Sheridan, J. & Rockwell, D. 2001 Forces and wake modes of an oscillating cylinder. *J. Fluids Struct.* **16**, 773–794.

Cheng, M., Chew, Y. T. & Luo, S. C. 2001*a* Numerical investigation of a rotationally oscillating cylinder in mean flow. *J. Fluids Struct.* **15**, 981–1007.

Cheng, M., Liu, G. R. & Lam, K. Y. 2001*b* Numerical simulation of flow past a rotationally oscillating cylinder. *Comput. Fluids* **30**, 365–392.

Chomaz, J.-M. 2005 Global instabilities in spatially developing flows. *Annu. Rev. Fluid Mech.* **37**, 357–392.

Choi, S., Choi, H. & Kang, S. 2002 Characteristics of flow over a rotationally oscillating cylinder at low Reynolds number. *Phys. Fluids* **14**, 2767–2777.

Chou, M.-H. 2001 Synchronization of vortex shedding from a cylinder under rotary oscillation. *Comput. Fluids* **26**, 755–774.

Fujisawa, N., Ikemoto, K. & Nagaya, K. 1998 Vortex shedding resonance from a rotationally oscillating cylinder. *J. Fluid. Struct.* **12**, 1041–1053.

Goujon-Durand, S., Jenffer, P. & Wesfreid, J. E. 1994 Downstream evolution of the Bénard–von Kármán instability. *Phys. Rev.* E **50**, 308–313.

Guilmineau, E. & Queutey, P. 2002 A numerical simulation of vortex shedding from an oscillating circular cylinder. *J. Fluids Struct.* **15**, 523–532.

He, J.-W., Glowinski, R., Metcalfe, R., Nordlander, A. & Periaux, J. 2000 Active control and drag optimization for flow past a circular cylinder. I. Oscillatory cylinder rotation. *J. Comput. Phys.* **163**, 83–117.

Jeon, D. & Gharib, M. 2004 On the relationship between the vortex formation process and cylinder wake patterns. *J. Fluid Mech.* **519**, 161–181.

Kang, S., Choi, H. & Lee, S. 1999 Laminar flow past a rotating cylinder. *Phys. Fluids* **11**, 3312.

Lu, X.-Y. & Sato, J. 1996 A numerical study of flow past a rotationally oscillating circular cylinder. *J. Fluids Struct.* **10**, 829–849.

Nishihara, T., Kanedo, S. & Watanabe, T. 2005 Characteristics of fluid dynamic forces acting on a circular cylinder oscillating in the streamwise direction and its wake pattern. *J. Fluids Struct.* **20**, 520–518.

Noca, F., Shiels, D. & Jeon, D. 1999 A comparison of methods for evaluating time dependent fluid dynamic forces on bodies, using only velocity fields and their derivatives. *J. Fluids Struct.* **13**, 551–578.

Poncet, P. 2002 Vanishing of mode B in the wake behind a rotationally oscillating circular cylinder. *Phys. Fluids* **14**, 2021–2023.

Poncet, P. 2004 Topological aspects of three-dimensional wakes behind rotary oscillating cylinders. *J. Fluid Mech.* **517**, 27–53.

Protas, B. & Styczek, A. 2002 Optimal rotary control of the cylinder wake in the laminar regime. *Phys. Fluids* **14**, 2073–2087.

Protas, B. & Wesfreid, J. E. 2002 Drag force in the open-loop control of the cylinder wake in the laminar regime. *Phys. Fluids* **14**, 810–826.

Protas, B. & Wesfreid, J. E. 2003 On the relation between the global modes and the spectra of drag and lift in periodic wake flows. *C R Méc.* **331**, 49–54.

Rockwell, D. 2000 Imaging of unsteady separated flows: global interpretation with particle image velocimetry. *Exps. Fluids* **29**, S255–S273.

Saffman, P. E. 1992 *Vortex Dynamics.* Cambridge University Press.

Sarpkaya, T. & Isaacson, M. 1981 *Mechanics of Wave Forces on Offshore Structures.* Van Nostrand Reinhold.

Shiels, D. & Leonard, A. 2001 Investigation of a drag reduction on a circular cylinder in rotary oscillation. *J. Fluid Mech.* **431**, 297–322.

Smith, D. R., Siegel, S. & McLaughlin, T. 2002 Modeling of the wake behind a circular cylinder undergoing rotational oscillation. *AIAA Paper 2002-3066, 1st AIAA Flow Control Conference, 24–26 June 2002/St Louis, MO.*

Taneda, S. 1978 Visual observations of the flow past a circular cylinder performing a rotatory oscillation. *J. Phys. Soc. Japan* **2**, 355–381.

Thiria, B. & Wesfreid, J. E. 2006 Stability properties of forced wakes. *J. Fluid Mech.* (submitted).

Tokumaru, P. T. & Dimotakis P. E. 1991 Rotary oscillation control of a cylinder wake. *J. Fluid Mech.* **224**, 77–90.

Wesfreid, J. E., Goujon-Durand, S. & Zielinska, B. J. A. 1996 Global mode behaviour of the streamwise velocity in wakes. *J. Phys. II* **6**, 1343–1357.

Williamson, C. H. K. & Roshko, A. 1988 Vortex formation in the wake of an oscillating cylinder. *J. Fluids Struct.* **2**, 355–381.

Zhu, Q., Wolfgang, M. J., Yue, D. K. P. & Triantafyllou, M. S. 2002 Three-dimensionnal flow structures and vorticity control in fish-like swimming. *J. Fluid Mech.* **468**, 1–28.

Zielinska, B. J. A. & Wesfreid, J. E. 1995 On the spatial structure of global modes in wake flow. *Phys. Fluids* A **7**, 1418–1424.

Zielinska, B. J. A., Goujon-Durand, S., Dusek, J. & Wesfreid, J. E. 1997 Strongly nonlinear effect in unstable wakes. *Phys. Rev. Lett.* **79**, 3893–3896.